Longitudinal Multi-Tensor Analysis of Neocortical Microstructure in an Animal Model of Cortical Dysplasia

Paulina J. Villaseñor [1], Hiram Luna-Munguía [1], Alonso Ramirez-Manzanares [2], Ricardo Coronado-Leija[3], and Luis Concha [1,*]

[1]Instituto de Neurobiología, Universidad Nacional Autónoma de México Campus Juriquilla, Querétaro, México
[2]Centro de Investigación en Matemáticas, A.C., Guanajuato, México
[3]Bernard and Irene Schwartz Center for Biomedical Imaging, New York University School of Medicine, New York, United States
[*]Corresponding author (lconcha@unam.mx)

Abstract

The neocortex is a highly organized structure, with region-specific spatial patterns of cells and fibers constituting cyto- and myelo-architecture, respectively. These architectural features are modulated during neurodevelopment, aging, and disease. While invasive techniques have contributed significantly to our understanding of cortical patterning, the task remains challenging through non-invasive methods. Structural magnetic resonance imaging (MRI) has advanced to improve sensitivity in identifying cortical features, yet most methods focus on capturing macrostructural characteristics, often overlooking critical microscale components. Diffusion-weighted MRI (dMRI) offers an opportunity to extract quantitative information reflecting microstructural changes. Here we investigate whether advanced multi-tensor dMRI methods can detect microstructural characteristics related to the orientational organization of the myelo- and cyto-architecture in an animal model of cortical dysplasia, a malformation of cortical development. We scanned 32 animals (n=16 experimental; n=16 control) at four different time points (30, 60, 120, and 150 post-natal days) using both structural and multi-shell dMRI. Our dMRI metrics were sampled using a 2D curvilinear system of coordinates as a common anatomical descriptor across animals. Diffusion tensors were labeled according to their orientation with respect to the cortical surface, and derived metrics were analyzed separately. We identified abnormalities in the perpendicular and parallel diffusion components in deeper cortical areas, consistent with histological findings of neuronal and fiber disorganization in animals with dysplasia. Although our methodology is tailored for small species, our protocol shows promise for clinical applications.

Keywords: diffusion-weighted imaging, gray matter, microstructure, immunofluorescent imaging, cortical dysplasia

1 Introduction

The architecture of the human cerebral cortex is complex, yet stereotypical. Billions of neurons and glial cells are precisely arranged in horizontal layers, with vertically-aligned neurons forming micro-columns (Lorente de Nó, 1938; Mountcastle, 1997; Rakic, 2009). A parallel cortical organization, termed myeloarchitecture, is created by the neuropil, with axons and dendrites running radially and tangentially to the cortical surface, supporting inter-columnar communication, as well as input and output to and from the cortex. Vogt & Vogt (1919) observed a consistent spatial arrangement of myelin across the cortex, albeit with variations in density and fiber length according to each cortical area (Nieuwenhuys, 2013). These spatially-varying histological patterns are complementary to the cytoarchitectonic areas described by Brodmann (1909), and are related to functional roles. Identification of cyto- and myelo-architectural patterns throughout the human neocortex—and their deviations from normality—has been relegated to invasive (and destructive) techniques. However, the examination of these patterns through non-invasive methods would provide valuable information for the study of cortical development and aging, as well as for the identification of alterations of cortical structure in neurological disorders.

Diffusion-weighted MRI (dMRI) provides a path to evaluate the cortex in vivo due to its ability to assess tissue properties at the micrometer scale by measuring the behavior of water displacement patterns over time. Though dMRI has been widely applied in white matter structures due to its ability to assess fiber orientations and tissue characteristics (Beaulieu, 2002; Concha, 2014; Le Bihan, 2003), advances related to image acquisition, pre-processing algorithms, the use of strong diffusion gradients, and novel computational methods have opened a new avenue to explore complex brain structures such as gray matter. Some have applied in vivo the diffusion tensor imaging (DTI) (Basser, 1994) in order to differentiate between the motor and somatosensory cortices by their anisotropy features (McNab et al., 2013) or to discriminate between cortical areas (Ganepola et al., 2018; Nagy et al., 2013). Others have investigated the myeloarchitectural laminar composition at high-resolution in the radial direction using ultra-high magnetic fields (Balasubramanian et al., 2021). However, it is well known that DTI has limitations, particularly in its ability to properly characterize complex microstructural configurations, such as the one in the cortex.

The multi-resolution discrete-search (MRDS) (Coronado-Leija et al., 2017) is a multi-tensor method that, contrary to the DTI, is able to fit up to three independent tensors for each voxel, thereby providing further information about the orientational microstructural components. The MRDS algorithm not only determines the optimal number of diffusion tensors to represent the underlying fiber configuration, but also independently estimates the main diffusion orientation and the diffusivity profile for each bundle. Additionally, the iterative use of dictionaries and non-linear optimization of the diffusion tensor makes MRDS robust and reliable, particularly at solving complex microstructural configurations, such as fibers crossing at an angle of $<45^\circ$.

Knowing that the cortex follows stereotypical horizontal and vertical dispositions, in this study, we aim to investigate 1) the ability of MRDS to identify the cortical orientational diffusion components in vivo, and 2) its histological correlation both in normal and abnormally-developed cortical microstructure. To this end, we used an animal model of cortical dysplasia (a common cause of pharmacologically-resistant focal-onset seizures in humans) (Benardete and Kriegstein, 2002; Moroni et al., 2011a), where rodents exhibit disrupted cortical columnar-layer organization and abnormal neuronal morphology.

2 Methods

2.1 Animal Model

All procedures were performed according to protocols approved by the Institute of Neurobiology UNAM ethics review board (file 111-A) and were carried out according to the Mexican Federal regulatory laws for animal experimentation (NOM-602-ZOO-1999).

To induce cortical lesions in our animal model similar to the ones seen in human cortical dysplasia (Najm et al., 2022), we used an antineoplastic chemical agent 1,3-Bis (2-chloroethyl) -1-nitrosourea (BCNU, also known as carmustine) that interferes with the replication of DNA, provoking mutagenesis on the neuronal proliferation during cortical neurodevelopment (Benardete and Kriegstein, 2002; Yamaguchi et al., 2010). We injected six Sprague-Dawley pregnant rats intraperitoneally with either BCNU (20 mg/kg; n=3) or saline solution for control (n=3) at embryonic day 15 (E15). Their offspring are the animals studied here (16 rats born to BCNU-treated dams and 16 born to saline-injected control dams), and were housed with their mothers until weaning in a room with a 12 h light/dark cycle with ad libitum access to food and water. Afterward, the animals were scanned at 30, 60, 120, and 150 post-natal days with our MRI protocols and processed for histology. BCNU-treated rats did not show any gross phenotypical or behavioral abnormalities compared to the controls and did not present spontaneous seizures, as expected in this animal model (Aquiles et al., 2023; Benardete and Kriegstein, 2002).

2.2 *In vivo* MRI acquisitions

Acquisition protocols were carried out at the National Laboratory of Magnetic Resonance Imaging using a 7 T Bruker animal scanner equipped with a 2×2 head coil and gradients with a maximum amplitude of 760 mT/m. Animals were first anesthetized with a mix of isoflurane (4% for induction and 2% for maintenance) and oxygen (2.5 l/min) during the entire scanning time while temperature and vital signs were monitored. We acquired anatomical T2-weighted images to assess the cortical morphology and diffusion-weighted images to describe the microstructure. Both sets of images were acquired in an orientation parallel to the coronal suture.

We obtained anatomical images using a T2-weighted TurboRARE sequence with TR/TE= 4212.78/33 ms and a spatial resolution of $0.117\times0.117\times1$ mm^3 (0.2 mm inter-slice gap). The acquisition time was 5 minutes.

Diffusion-weighted images were acquired with pulsed gradient diffusion sensitization in 90 different directions, each one with b values of 670, 1,270, and 2010 s/mm^2, with diffusion gradient duration $\delta = 3$ ms and separation $\Delta = 9$ ms. Fourteen $b = 0$ s/mm^2 images were also acquired. The sequence used an echo-planar (EPI) readout with the following parameters TR/TE=2000/22.86 ms and spatial resolution of $0.175\times0.175\times1.0$ mm^3 (0.25 mm inter-slice gap). The scan time was 19 minutes.

2.3 Diffusion-MRI analysis

Diffusion-weighted images were first pre-processed using tools available in MRtrix3 (ver. 3.0.3) and FSL (ver. 6.0.2) by: 1) removing signal noise (Veraart et al., 2016), 2) reduction of distortions induced by eddy currents (Andersson et al., 2003), and 3) bias field correction (Tustison et al., 2010).

Once images were pre-processed, for each animal we manually delineated the superior (pial surface) and the inferior (intersection between the gray and white matter) cortical borders in a single slice at the level of the dorsal hippocampus (Bregma 5.86 - 3.14 mm), using the software ITK-SNAP (Yushkevich et al., 2006). Next, we created a standardized curvilinear grid to describe the cortex by fitting a Laplacian field within the manually-defined boundaries (Lerch et al., 2008) (Figure 1A; panels i-ii); further details are described in (Villaseñor et al., 2023).

For the dMRI analysis, we independently fit (i) a single diffusion tensor (i.e., DTI) (Basser, 1994) and (ii) multiple tensors using MRDS (Coronado-Leija et al., 2017) at each temporal time point (Figure 1A; panel iii-iv). For the MRDS implementation, we fitted up to three independent tensors per voxel, each one with its own diffusivity profile (eigenvalues) and orientation (eigenvectors). To determine the parameters of the intra-voxel mixture of tensors, the MRDS algorithm selects the orientations from a dictionary and then applies numerical optimization techniques and a discrete search to fit the best eigenvalues. Next, the Bayes' information criterion is used to determine the multi-tensor configuration that best explains the diffusion signal. We set 30° as the minimum angle possible between the first eigenvectors of two independent tensors. From MRDS we obtained fractional anisotropy (per-bundle FA) and mean diffusivity (per-bundle MD) for each of the identified tensors per voxel, which were later labeled according to their main orientation with respect to the grid lines that traverse the cortical mantle. Namely, we calculated the dot product between the normalized principal diffusion direction of each tensor with respect to the (normalized) closest grid line segment. The eigenvector with the highest normalized absolute dot product was designated as parallel ($_{par}$), while the eigenvector with the lowest normalized dot product was labeled as perpendicular ($_{perp}$). If more than two tensors were identified at a given voxel, the most perpendicular tensor with respect to the grid-lines was reported as perpendicular.

2.4 Statistical analysis

For each vertex in the grid-lines, we performed a Linear Mixed-Effects Model (LMM) analysis using R (ver. 4.1.0). The model was fitted with the response variable (Y) being each one of the diffusion metrics, with explanatory variables being the temporal time points and experimental group as fixed-effects (β), and each of the animals as the mixed-effects (γ).

Estimated marginal means and post hoc tests were calculated. Given the multiple statistical tests, we adjusted the significant p-value by permuting and recalculating the LMM test at each vertex (5,000 permutations). Then, cluster-wise statistical inference was performed by computing the empirical null distribution of cluster sizes after the 5,000 permutations with a threshold of $p<0.05$ with four-point connectivity (following the ideas behind AFNI's *3dclustsim* (Cox et al., 2017)). Lastly, effect sizes were estimated with Cohen's f^2 at each point (Figure 1B).

2.5 Histological validation

2.5.1 Immunofluorescence

For our histological procedure, we sacrificed two animals from each group at each time point (P30, P60, P120, and P150). Animals were transcardially perfused with a 0.9% NaCI solution followed by a 4% paraformaldehyde (PFA) solution (pH 7.4). Subsequently, their brains were removed and post-fixed in fresh 4% PFA solution for 24 h at 4 °C. Following fixation, the brains were immersed until sinking in 20% and 30% sucrose solution at 4°C for 48 h. Finally, brains were frozen using dry ice and stored at -80 °C.

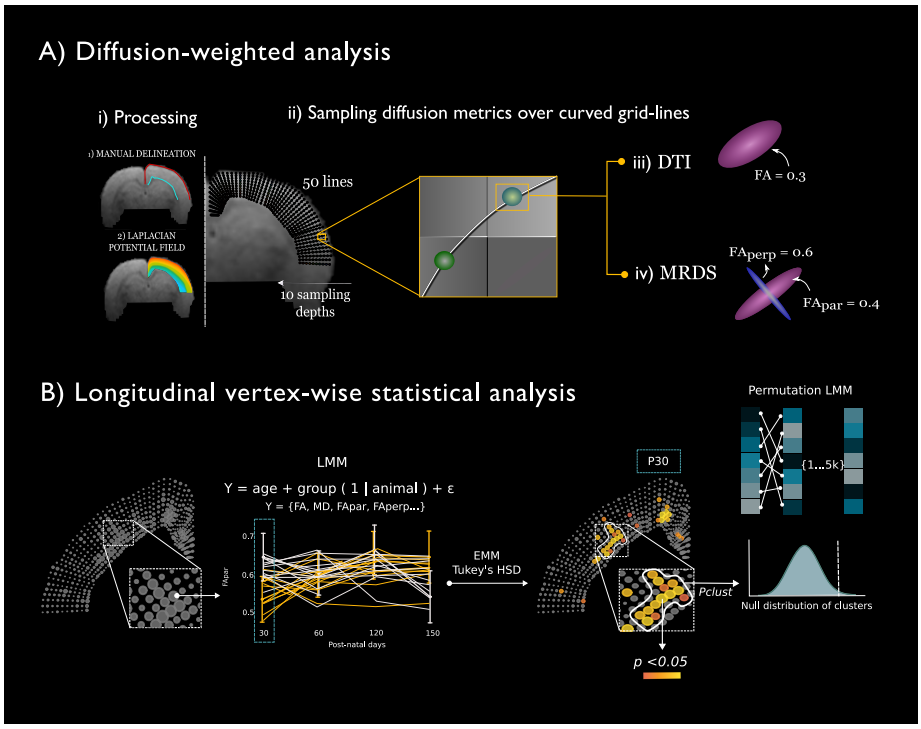

Figure 1: *Workflow of dMRI processing and statistical analysis. A) Images were first i) processed with a manual delineation of the external and internal cortical border followed by the application of a Laplacian potential field to create the grid-lines (fifty lines and ten points each); ii) At each vertex we sample diffusion metrics derived from diffusion tensor (iii) and multi-resolution discrete-search method (MRDS, iv). B) A linear mixed effect model (LMM) was fitted at each vertex for each diffusion metric (Y). This was followed by the estimation of marginal means and Tukey's correction for the significant p-value <0.05 (yellow-orange scale). Cluster-based correction for multiple comparisons was performed by permutations (white contours).*

Prior to the staining process, brains were sectioned in the coronal plane (20 µm thick), at the level of the dorsal hippocampus (Bregma 5.86 - 3.14 mm) using a Leica Biosystems 3050S cryostat. The series of sections were stored in 1X phosphate buffer solution (PBS; Sigma-Aldrich) until the immunofluorescence staining. For blocking, we immersed the brain slices for 45 minutes at 4 °C in 2% Bovine Serum Albumin solution (BSA; Sigma-Aldrich) and 0.3% triton X-100 (ThermoFisher) in 1X PBS. To characterize cytoarchitecture, we employed the primary antibody anti-mouse Neuronal Nuclei (NeuN; 1:350; Abcam). For assessing the myeloarchitecture, we performed a double immunofluorescence staining by using the following primary antibodies: anti-rabbit Myelin Basic Protein (MBP; 1:200; Sigma-Aldrich) and anti-mouse Neurofilament 200 (NF200; 1:200; Sigma-Aldrich). All primary antibodies were incubated for 24 hours at 4 °C and subsequently rinsed three times with 1X PBS for 10 minutes each. Following primary antibody incubation, the corresponding secondary antibodies (Alexa Fluor) goat anti-rabbit 555 (1:500) and goat anti-mouse 488 (1:500) were incubated for 4 hours at 4 °C. The slices were then rinsed three times with 1X PBS for 10 minutes each. Finally, slices were cover-slipped with microscope cover glass.

2.5.2 Image processing and structure tensor

Brain slices were captured using a fluorescence Apotome-Zeiss microscope equipped with 565 and 488 nm emission filters. The microscope was connected to a console integrated with the AxioVision software (ver 4.8). Mosaics encompassing the entire slice were created by stitching individual tiles captured with a 10X objective using the MosaiX module available in AxioVision.

Imaging processing was performed using the FIJI software (ver. 2.15.0). Initially, images were processed for background removal and adjustments to brightness and contrast for improved visualization. For the channel showing fluorescence associated with MBP, we implemented the structure tensor analysis using the OrientationJ plugin (Püspöki et al., 2016) which is designed to calculate the primary orientation for a specified number of pixels. A Gaussian kernel of 5 µm was utilized to compute the structure tensor, estimating orientation and anisotropy from a local neighborhood. The coherency parameter was then calculated, defined as the ratio between the difference and the sum of the eigenvalues. Akin to the diffusion tensor's FA, coherency maps represent the degree of local tissue orientation, with a coherency value of 1 indicating the presence of a dominant orientation (i.e., anisotropy) in the image, while a value of 0 signifies completely incoherent orientations within the local neighborhood (Clemons et al., 2018).

3 Results

3.1 Structural MRI

In Figure 2, we present a comparison of two sectional coronal slices at the level of the somatosensory cortex and the hippocampus (anteroposterior -0.4 mm and -3.14 mm, respectively from Bregma; coordinates taken from the atlas rat brain of Paxinos and Watson). At P30, no evident morphological differences between groups was observed. However, on the following time points, BCNU-treated rats exhibited notable changes, including enlarged ventricles and subsequent hippocampal atrophy. Moroni & Zucca (Moroni et al., 2011b) reported similar hippocampal lesions in their overview detection of cortical dysplasia in adult BCNU-treated rats. In our study, these abnormalities displayed a progressive trend over time, extending to the ventral hippocampus. Interestingly, the lesions in the ventricles were not uniformly distributed among BCNU-treated rats. Each animal showed variations in severity and location, with some showing either uni- or bilateral abnormalities. This variability suggests that animals from the BCNU group may possess inherent variations in characteristics of cortical dysplasias during their development.

3.2 Diffusion-MRI analysis

Our analysis from the DTI revealed no significant differences in the spatial distribution of diffusion metrics between groups at any of the time points evaluated (Figure 3A). However, when examining individual vertices to assess the relationship between metrics and postnatal days calculated from the linear mixed effect model (LMM), we observed that, as compared to controls, BCNU-treated rats tended to have lower values of MD, AD, and RD. Interestingly, BCNU-treated rats showed slightly higher FA values when compared to control rats (Figure 3B); not exceeding 0.3, as expected for the cortex. On top, the effect size (f^2) lacks strength, with a maximum value of 0.08, indicating a shallow effect between animals across vertices.

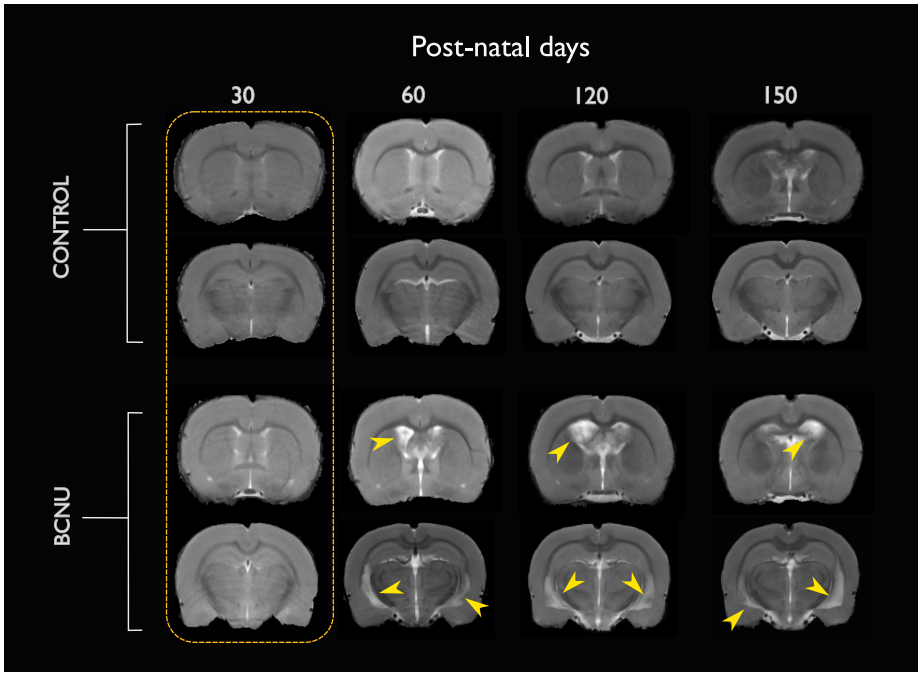

Figure 2: *T2-weighted coronal images taken at two different levels: somatosensory cortex and the dorsal hippocampus. At P30 (yellow rectangle) there were no apparent gross morphological differences between groups. BCNU-treated rats revealed progressive enlargement of the ventricles and hippocampal atrophy from P60 to P150 (yellow arrowheads).*

On the other hand, MRDS analysis showed changes in diffusivities between groups (Figure 4). In the case of FA_{par}, changes were observed in the somatosensory and motor cortex at the level of the deepest cortical layer IV-VI at P30. Interestingly, these changes were not evident between P60 and P120, arising again at P150, with a cluster of significant vertices located in similar cortical regions as seen at P30. An illustrative individual vertex analysis (Figure 4B) showed that at P30, control animals achieved FA_{par} values of up to 0.7, while BCNU-treated animals maintained lower anisotropy in the parallel direction. FA_{perp} followed a similar trend, with significant differences in the tangential direction in the cortex. Between groups, a strong spatial-cluster relation encompassed the cortical layers V and VI in both the somatosensory and motor cortex. However, these differences were only observed at P30, with no significant clusters in later postnatal days. MD_{perp} showed spread-out significant vertices across ages but without a clear spatial clustering. Contrarily, MD_{perp} pinpointed a cluster of vertices around the layers V-VI at P30 and another in more superficial layers (IV-II) at P60. The right panel shows how BCNU-treated animals had higher values in MD_{perp}, which could be indicative of cell-size abnormalities, as observed in Figure 5.

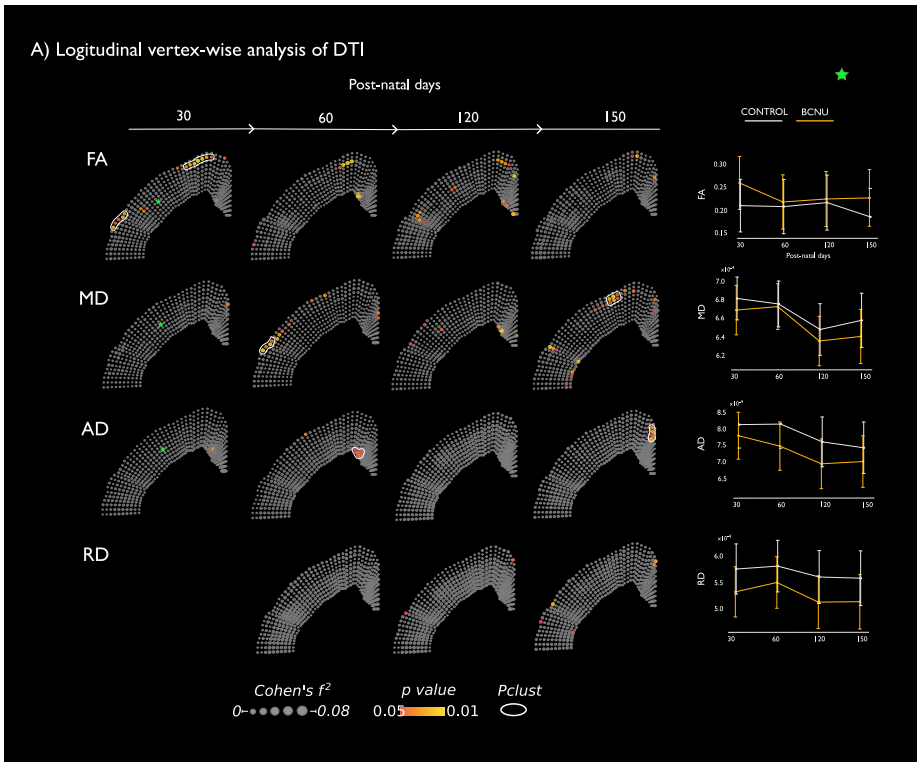

Figure 3: *Vertex-wise DTI analysis of the cortex. A) Visualization of the resulting statistical analysis. Significant point-wise post hoc between-group differences (p<0.05) are represented in yellow-orange scale; non-significant in gray, with effect size represented as marker size. DTI metrics differ minimally between groups over time. FA and MD metrics exhibited a few significant clusters (pclust<0.05; delineated in white) primarily in the most superficial cortical layers, while AD and RD did not show significant group differences. B) Individual vertex (green star, panel A) analysis demonstrates the effect of predictors over time for each metric between groups (control in white, BCNU in yellow; mean and confidence intervals).*

3.3 Histological validation and Structure Tensor analysis

3.3.1 Cytoarchitecture

The NeuN-stained images yielded valuable features about the six-layered neuronal organization. Here, animals with cortical dysplasia showed an evident disruption of the transition between layers and their radial orientation. This abnormal pattern was evident throughout the entire brain of BCNU-treated rats, with certain cortical regions displaying more pronounced disorganization than others. Figure 5A presents a close-up examination of the somatosensory cortical layering from both groups. Control animals preserved a clearly defined transition across layers, with each layer showing distinct cell density, morphology, and size. On the other hand, BCNU-treated rats exhibited a blurred delineation between layers III-IV and V-VI, as indicated by the color-coded lines (Figure 5; i). These alterations in lamination were consistently observed across all the evaluated time points.

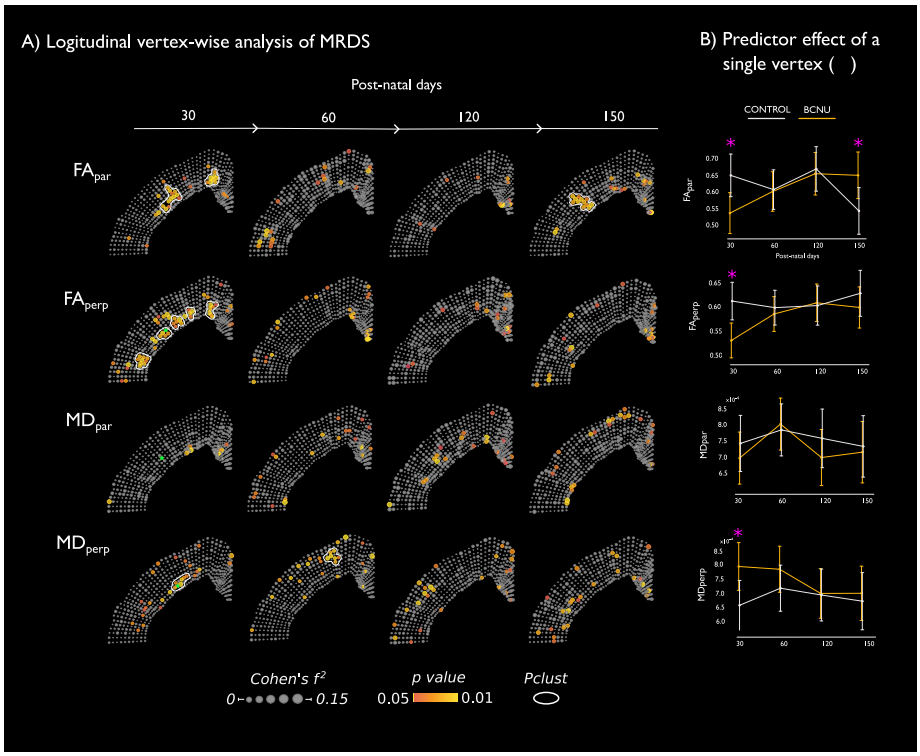

Figure 4: *Vertex-wise MRDS analyses. A) At early stages of development (P30) FA_{par}, FA_{perp}, and MD_{perp} revealed significant changes (pclust<0.05; delineated in white) of the somatosensory and motor cortices, primarily affecting the cortical layers VI-IV. MD_{perp} displayed no abnormalities over time. At P150, FA_{par} was the only metric showing abnormalities significant at the cluster level. B) In the single vertex (green star, panel A) analysis, control animals exhibited higher values in FA_{par} and FA_{perp} compared to BCNU-treated rats (magenta asterisks). Only MD_{perp} showed higher levels in BCNU-treated animals relative to controls at P30 (plots show the mean and confidence intervals).*

However, cortical disarray not only impacted the layer organization but also affected columnar assembling, as seen in Figure 5-ii. In control animals, chains of neurons followed a radial orientation from the deepest layer (VI) to the superficial layer II over time after birth. On the contrary, BCNU-treated rats showed not only a disorganized vertical orientation, but also a reduction in cell density, particularly in layer V, and an increased cell body size, with the most pronounced effects observed at P60. Such important changes in cytoarchitecture, affecting both orientation and cell morphology, likely drive alterations in the parallel and perpendicular diffusion components, as evidenced by changes in FA_{par}, FA_{perp}, and MD_{perp}.

3.3.2 Myeloarchitecture

Our examination of myelin-stained samples provided valuable insights into the microstructural organization of intra-cortical fibers. Using the structure tensor analysis workflow, we investigated

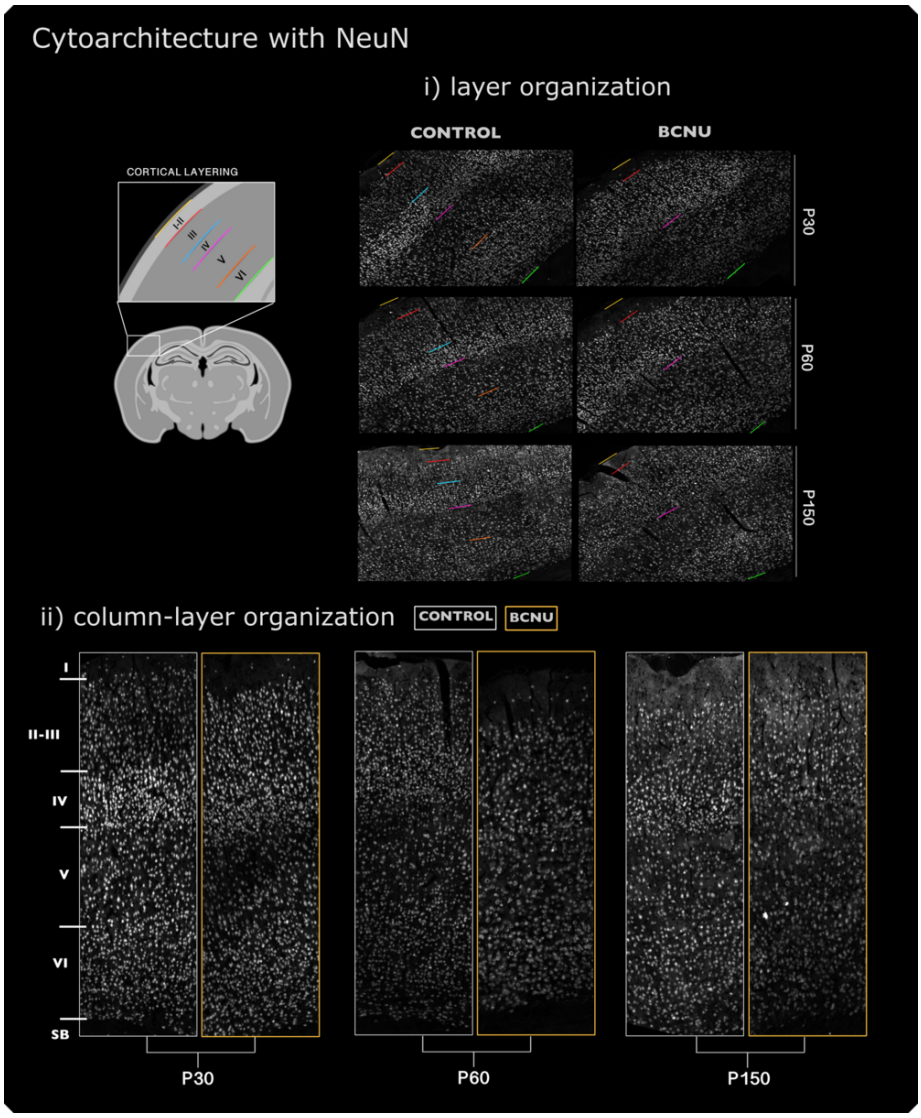

Figure 5: *Cytoarchitecture of the somatosensory cortex. Coronal sections at the level of the dorsal hippocampus stained with NeuN revealed alterations in their layering organization. Each layer was delineated by color-coded lines (i; left panel). The right panel shows BCNU-treated rats displaying a blurred distinction between cortical layers III-IV (cyan line) and V-VI (orange line) over time after birth, in contrast to control animals. A closer examination of columnar-layer organization (ii) evidences a clear layer differentiation in control rats (white rectangle) accompanied by radial neuronal orientation. BCNU-treated rats (yellow rectangle) displayed a series of abnormalities including disorganized vertical orientation, decreased cellular density across layer V, and enlarged cell body size.*

the fiber structure in both groups by computing the coherency maps (Figure 6A), and staining for myelin (green) and neurofilament (red) to elucidate their potential impact on cortical diffusivities.

Coherency maps derived from myelin staining (Figure 6B; left panel) depicted consistent anisotropic patterns in cortical layers IV and VI in control animals, with slight age-dependent variation in intensity. However, in the BCNU-treated sample at P30, a significant cortical area displayed abnormal hyperintensity spanning from layer IV to I, accompanied by a loss of orientation in the deeper layers V and VI. Corresponding myelinated fibers taken from the somatosensory cortex exhibited radial and intracortical fiber disarrangement in the BCNU-treated rat, being consistent with the results derivatives from the multi-tensor, where FA_{par}, FA_{perp}, and MD_{perp} displayed major changes in the radial and tangential diffusivities. While pronounced changes in primary orientation were evident at P30, similar alterations persisted in subsequent developmental stages. At P60, differences in coherence were notable, particularly at the white and gray matter boundary, possibly influenced by ventricular enlargement (marked with a white asterisk). In older stages such as P120 and P150, subtle disorganization of myelin fibers was observed in BCNU-treated rats compared to controls. However, regardless of postnatal day, all animals with cortical dysplasia shared a common feature: disorganized myelin fibers in cortical layers V and VI. No discernible changes were noted in neurofilament organization between groups (Figure A.1).

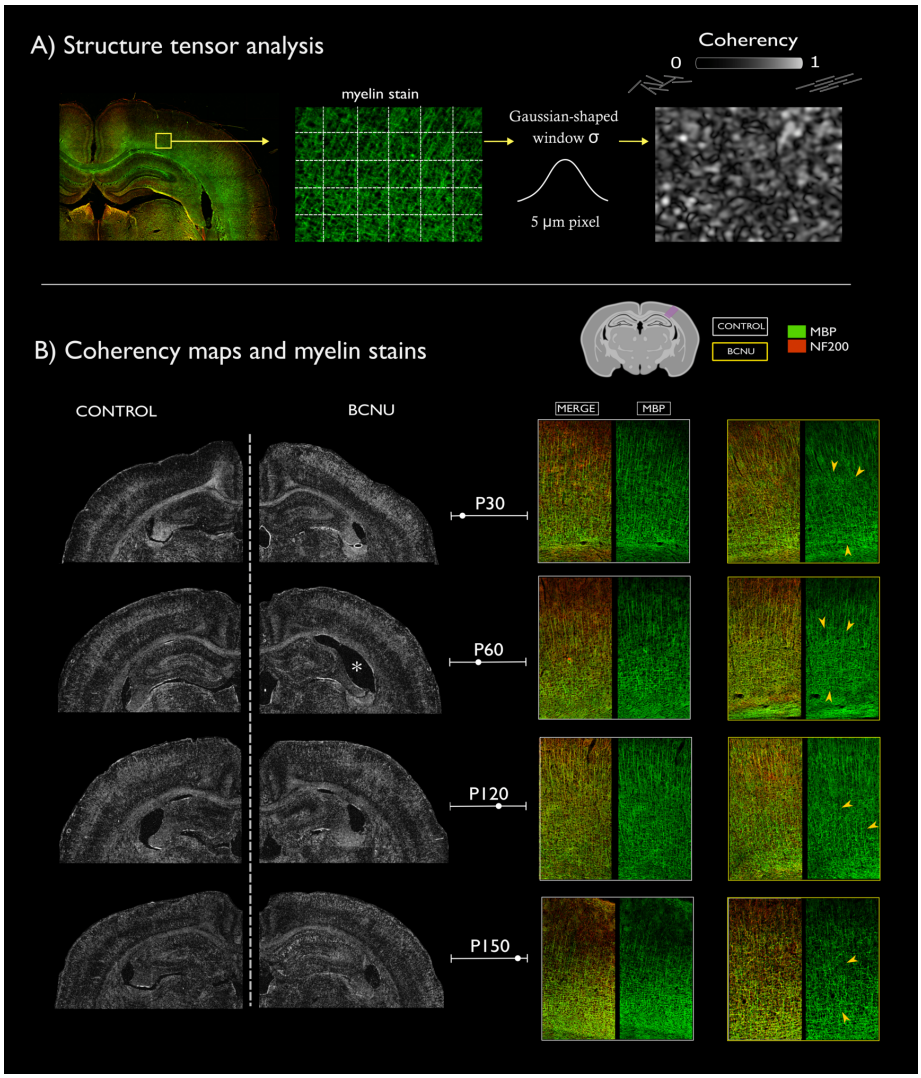

Figure 6: *Evaluation of myeloarchitecture. A) MBP stains (in green) were used to estimate coherency maps through structure tensor analysis. The resulting maps are visualized using a gray scale: brighter regions indicate higher fiber organization (i.e., anisotropy), and darker regions represent lower textural coherence. B) BCNU-treated rats exhibited decreased coherence between the white and gray matter boundaries, particularly at P30 (arrows). Myelin-stained sections from the somatosensory cortex (right panel) revealed disrupted myelin fiber arrangements (yellow arrows) in layers VI and V of BCNU-treated rats (yellow boxes) compared to control animals (white boxes).*

4 Discussion

The cerebral neocortex comprises a highly organized arrangement of cells and fibers, rendering it a complex structure that supports high-level functions. While histology has yielded profound insights into cortical microstructure, challenges persist in achieving microstructural specificity through in vivo MRI. This limitation not only poses hurdles to scientific inquiry but also hinders clinical applications aimed to detect cortical abnormalities at the microscale level. In this study, we provide evidence supporting the use of a multi-tensor dMRI method to detect cortical orientational microstructural components in a rat model of cortical dysplasia.

The MRI signal arises from the contribution of all tissue components in any given voxel. However, by providing sensitivity to specific intrinsic features, major advances have been made to enhance the visualization of cortical structures. For instance, parcellation of cortical areas based on contrast intensity from T1- or T2-weighted images enabled differentiation between cortical areas, measurement of cortical thickness, and visualization of myelination across the cortical surface (Bock et al., 2009; Fischl et al., 2004; Glasser and Essen, 2011). Other advanced methods such as high-resolution MRI have revealed laminar patterning features associated with myelin and cellular density within specific cortical areas (Eickhoff et al., 2004; Walters et al., 2003). However, these methods still primarily capture structural aspects, often overlooking important microstructural characteristics at the sub-voxel level, particularly relevant for studying normal and abnormal neurodevelopment, and cortical degeneration due to aging or neurological disorders.

Diffusion-weighted MRI (dMRI) opened an important avenue for non-invasive tissue exploration beyond macrostructural features. While most dMRI methods have focused on studying white matter bundles and structural brain connectivity, there is a growing trend toward unraveling the complexity of the cortex. The neuropil (i.e., the space between neurons and glial cells, including axons, dendrites, and microvasculature) (Spocter et al., 2012), has such an intricate organization that it is expected to show little diffusion anisotropy through conventional dMRI methods (Kroenke, 2018). However, despite lacking large-caliber axons like those in white matter, the histological configuration of the neocortex is not isotropic. In contrast, the dense radial and perpendicular arrangement of neurons and myelinated fibers could potentially contribute to the anisotropic diffusion of the cortex (Beaulieu, 2002; Reveley et al., 2022). For instance, cortical regions with well-defined columnar and layer boundaries, such as the motor and somatosensory cortices, have been parcellated by fitting the single diffusion tensor (DTI) (Ganepola et al., 2018; McNab et al., 2013; Nagy et al., 2013; Basser, 1994). Previous studies have also shown a strong radial diffusion component inside the cortex with variations of the tangential orientation across cortical areas (Assaf, 2019; Leuze et al., 2014; McNab et al., 2013). Our work shows that multi-tensor analysis of the diffusion signal can disentangle the contribution of fibers that run radial or tangential to the cortical surface in the rodent brain, surpassing the limitations inherent in single-tensor techniques. While not directly tested in this work, other methods that are able to resolve per-bundle orientations and architectural features, such as constrained spherical deconvolution (CSD)(Tournier et al., 2007), should also be adequate for this task (Leuze et al., 2014). Our choice of MRDS for this study relies on its simple biological interpretation through metrics such as FA and MD, here differentiated according to their orientation relative to the cortical surface.

In recent years, there has been growing interest in evaluating tissue microstructure by modeling the dMRI signal according to prototypical biophysical compartments. Several biophysical models have been proposed in order to identify white matter characteristics like axonal radius, intra- and extra-axonal diffusivities, and their relative volume fraction (Alexander et al., 2010; Assaf, 2019;

Novikov et al., 2018b; Zhang et al., 2012) proving to be useful for the study of neurodegenerative diseases (Andica et al., 2020). However, modeling the cortex is less straightforward due to the broader components found in gray matter (i.e. glia, neurons, and fibers). Previous studies have applied neurite orientation dispersion and density imaging (NODDI)(Zhang et al., 2012) to investigate microstructural variations in the cortex (Fukutomi et al., 2018, 2019), changes in the neurite dispersion in chronic psychosis spectrum disorders (Kraguljac et al., 2023; Nazeri et al., 2017), and also in focal cortical dysplasia were they reported a reduced intracellular volume (Lorio et al., 2020). Similarly, multidimensional tensor encoding has been useful for enhancing the delineation of cortical malformations by differentiating between gray and white matter boundaries (Lampinen et al., 2020). New advanced methods offer further steps toward gray matter characterization by measuring soma and neurite density (SANDI) (Palombo et al., 2020), and recognizing the important role of time-dependence and exchange diffusion (NEXI) (Jelescu et al., 2022) in the cortex. However, to capture the signal contributions for each compartment, high acquisition requirements are needed, including several diffusion sensitizations (up to 5 shells) and very high b-values (>10,000 s/mm^2), resulting in lengthy scanning times. Notably, both SANDI and NEXI remove the orientational information by powder-averaging the signals. Here. MRDS offers several advantages due to its relatively accessible acquisition requirements, feasible scanning times, and its ability to provide per-bundle diffusion metrics. Moreover, MRDS, being a signal representation rather than a model (Novikov et al., 2018a), does not rely on any assumptions about the underlying microstructure. While MRDS may not explicitly compartmentalize diffusion, our findings regarding FA_{par}, FA_{perp}, and MD_{perp} (Figure 4) in the cortex demonstrate a discernible differentiation between normal and abnormal microstructural orientational components.

In this work, we show that MRDS is able to detect abnormalities of cortical microstructure even in the absence of gross morphological alterations. This becomes particularly relevant for the detection of very subtle cortical alterations that can nonetheless cause severe neurological disorders, such as medically-refractory epilepsy due to focal cortical dysplasia (Bernasconi et al., 2011). To prove the validity of our methodological approach, we used an animal model of FCD which, through the administration of carmustine (BCNU) during a critical stage of cortical development, causes histological disarrangement of the cortex with features akin to those seen in FCD Type II (Blümcke et al., 2011). While newer animal models of FCD better reflect the electrophysiological properties of these malformations of cortical development (Luhmann, 2016; Nguyen and Bordey, 2022; Wong, 2009), the BCNU model used here serves as a valid proxy for their histological abnormalities and a good fit for their detection with dMRI. Our longitudinal design further allowed us to evaluate the trajectories of these changes over time. In previous studies, T2-weighted images have shown that BCNU-treated rodents displayed macrostructural abnormalities such as ventricular enlargement and hippocampal atrophy at P60 (Inverardi et al., 2013; Moroni et al., 2011b,a), similar to those depicted in Figure 2. However, in this study, while the progressive evolution of ventricular enlargement and atrophy became apparent from P60 onwards, animals at earlier developmental stages (P30) did not exhibit any gross morphological abnormalities. Microscopic developmental changes often go unnoticed in anatomical images. For example, during early development, fiber organization and maturation of oligodendrocytes can be reflected in a progressive increase in anisotropy and a decrease in overall diffusivity (Drobyshevsky et al., 2005; Yoshida et al., 2013). Nevertheless, our results with a decreased FA_{par}, FA_{perp}, and an increased MD_{perp} at P30 (Figure 4) suggest that BCNU-treated rats present a disruption in their cortical maturation during critical developmental periods, and potentially reach a plateau in later postnatal ages. Such observations were consistent with our histological findings, where radial and tangential fiber disorganization was detected in

myelin-stained samples in BCNU-treated rats (Figure 6). Although higher values in mean diffusivity have been linked to neurodegenerative diseases, the increased MD_{perp} in BCNU-treated rats could be attributed to both a loss of myelinated fibers projected in the tangential plane and the lack of boundaries between each cortical layer, as demonstrated in Figure 5.

The current study encompasses several considerations. Firstly, it involves the direct application of MRDS in the cortex, when the method was originally designed for the analysis of white matter. While MRDS has demonstrated robustness in estimating tensors in areas with crossing fibers (Coronado-Leija et al., 2017; Rojas-Vite et al., 2019), its reliability in gray matter remains a subject of inquiry. However, our prior investigation (Villaseñor et al., 2023) supports evidence that MRDS can detect changes of cortical organization at the early stages of development. Secondly, this study undertook a longitudinal analysis involving the sacrifice of four animals (n=2 Control; n=2 BCNU) at each temporal point. This approach introduces two implications: 1) the reduced number of samples at each point that could impact the statistical analysis, and 2) the lack of one-to-one correlation between total dMRI metrics and histology. Thirdly, while our images possess high spatial resolution in-plane, slice thickness is relatively large (1 mm), thereby introducing partial volume effects in our dMRI estimations. Next, while MRDS can fit up to three tensors, in this analysis we only included the most parallel and most perpendicular tensors with respect to the grid-line. These perpendicular tensors could have a medial-to-lateral orientation, or run orthogonal to the imaging plane. The distinction between these two forms of intra-cortical diffusivities (i.e., intracortical fibers) was not attempted due to the aforementioned thick slices. Finally, the spatial resolution afforded by pre-clinical scanners is much higher than what can be attained presently with clinical scanners. On the other hand, the possibility of dMRI to discern structural features within-voxel, advances in high-performance gradients (Fan et al., 2022), and the advent of super-resolution techniques (Coupé et al., 2013; Luo et al., 2022) will propel the adoption of dMRI for the study of neocortical features.

Our study offers compelling evidence that MRDS can discern microstructural abnormalities associated with abnormal organization of cortical layers and columns. Moreover, it proves useful for separating and identifying the orientational cortical components of cyto- and myelo-architecture. While this study is preclinical in nature, our findings underscore the potential of utilizing dMRI and advanced multi-tensor methods for clinical applications where neocortical histopathology is suspected.

4.1 Authors contributions

PJV, HL-M, AR-M, and LC contributed to the conception, methodology, and design of the study. HL-M and PJV performed experiments and imaging acquisition. PJV performed dMRI statistical analysis, histological procedures, and structure tensor analysis. RC-L provided the MRDS code and supervised the analysis of diffusion. PJV and LC wrote, reviewed, and edited the first manuscript. All authors reviewed the manuscript and approved the submitted version.

4.2 Acknowledgments and Funding

We thank Mirelta Regalado, Juan Ortiz-Retana, Nydia Hernández-Ríos, Ericka de los Ríos, Lourdes Palma, Gema Martínez, and Leopoldo González-Santos for their technical assistance. We also thank the personnel at the Animal Facility: Martin Garcia, Alejandra Castilla, Maria A. Carbajo, and Maria E. Ramos. This research was funded by UNAM-DGAPA- PAPIIT (IN2044720 and IN213423

for LC; IA200621 and IN224523 for HL-M) and CONAHCYT (CF-218-2023). MRI preclinical scanner facilities were provided by the National Laboratory of Magnetic Resonance (LANIREM), which receives support from CONAHCYT and UNAM. Computing infrastructure was partially provided by the National Laboratory for Advanced Scientific Visualization (LAVIS). Paulina J. Villaseñor received a scholarship from CONAHCyT (798166). AR-M was partially supported by CONAHCYT.

5 References

References

Alexander, D. C., Hubbard, P. L., Hall, M. G., Moore, E. A., Ptito, M., Parker, G. J. M., and Dyrby, T. B. (2010). Orientationally invariant indices of axon diameter and density from diffusion mri. *NeuroImage*, 52(4):1374–1389.

Andersson, J. L. R., Skare, S., and Ashburner, J. (2003). How to correct susceptibility distortions in spin-echo echo-planar images: application to diffusion tensor imaging. *NeuroImage*, 20(2):870–888.

Andica, C., Kamagata, K., Hatano, T., Saito, Y., Ogaki, K., Hattori, N., and Aoki, S. (2020). Mr biomarkers of degenerative brain disorders derived from diffusion imaging. *Journal of Magnetic Resonance Imaging*, 52(6):1620–1636.

Aquiles, A., Fiordelisio, T., Luna-Munguia, H., and Concha, L. (2023). Altered functional connectivity and network excitability in a model of cortical dysplasia. *Scientific Reports*, 13(1):12335.

Assaf, Y. (2019). Imaging laminar structures in the gray matter with diffusion mri. *NeuroImage*, 197:677–688.

Balasubramanian, M., Mulkern, R. V., Neil, J. J., Maier, S. E., and Polimeni, J. R. (2021). Probing in vivo cortical myeloarchitecture in humans via line-scan diffusion acquisitions at 7 t with 250-500 micron radial resolution. *Magnetic Resonance in Medicine*, 85(1):390–403.

Basser, P. J. (1994). Estimation of the effective self-diffusion tensor from the nmr spin echo - pubmed.

Beaulieu, C. (2002). The basis of anisotropic water diffusion in the nervous system - a technical review. *NMR in biomedicine*, 15(7–8):435–455.

Benardete, E. and Kriegstein, A. (2002). Increased excitability and decreased sensitivity to gaba in an animal model of dysplastic cortex. *Epilepsia*, 43(9):970–982.

Bernasconi, A., Bernasconi, N., Bernhardt, B. C., and Schrader, D. (2011). Advances in mri for "cryptogenic" epilepsies. *Nature Reviews. Neurology*, 7(2):99–108.

Blümcke, I., Thom, M., Aronica, E., Armstrong, D. D., Vinters, H. V., Palmini, A., Jacques, T. S., Avanzini, G., Barkovich, A. J., Battaglia, G., et al. (2011). The clinicopathologic spectrum of focal cortical dysplasias: A consensus classification proposed by an ad hoc task force of the ilae diagnostic methods commission 1.

Bock, N. A., Kocharyan, A., Liu, J. V., and Silva, A. C. (2009). Visualizing the entire cortical myelination pattern in marmosets with magnetic resonance imaging. *Journal of Neuroscience Methods*, 185(1):15–22.

Brodmann, K. (1909). *Vergleichende Lokalisationslehre der Grosshirnrinde in ihren Prinzipien dargestellt auf Grund des Zellenbaues*. Barth.

Clemons, T., Bradshaw, M., Toshniwal, P., Chaudhari, N., Stevenson, A., Lynch, J., Fear, M., Wood, F., and Iyer, K. S. (2018). Coherency image analysis to quantify collagen architecture: implications in scar assessment. *RSC Advances*, 8(18):9661–9669.

Concha, L. (2014). A macroscopic view of microstructure: using diffusion-weighted images to infer damage, repair, and plasticity of white matter. *Neuroscience*, 276:14–28.

Coronado-Leija, R., Ramirez-Manzanares, A., and Marroquin, J. L. (2017). Estimation of individual axon bundle properties by a multi-resolution discrete-search method. *Medical Image Analysis*, 42:26–43.

Coupé, P., Manjón, J. V., Chamberland, M., Descoteaux, M., and Hiba, B. (2013). Collaborative patch-based super-resolution for diffusion-weighted images. *NeuroImage*, 83:245–261.

Cox, R. W., Chen, G., Glen, D. R., Reynolds, R. C., and Taylor, P. A. (2017). fmri clustering and false-positive rates. *Proceedings of the National Academy of Sciences of the United States of America*, 114(17):E3370–E3371.

Drobyshevsky, A., Song, S.-K., Gamkrelidze, G., Wyrwicz, A. M., Derrick, M., Meng, F., Li, L., Ji, X., Trommer, B., Beardsley, D. J., Luo, N. L., Back, S. A., and Tan, S. (2005). Developmental changes in diffusion anisotropy coincide with immature oligodendrocyte progression and maturation of compound action potential. *Journal of Neuroscience*, 25(25):5988–5997.

Eickhoff, S., Walters, N. B., Schleicher, A., Kril, J., Egan, G. F., Zilles, K., Watson, J. D., and Amunts, K. (2004). High-resolution mri reflects myeloarchitecture and cytoarchitecture of human cerebral cortex. *Human Brain Mapping*, 24(3):206–215.

Fan, Q., Eichner, C., Afzali, M., Mueller, L., Tax, C. M. W., Davids, M., Mahmutovic, M., Keil, B., Bilgic, B., Setsompop, K., Lee, H.-H., Tian, Q., Maffei, C., Ramos-Llordén, G., Nummenmaa, A., Witzel, T., Yendiki, A., Song, Y.-Q., Huang, C.-C., Lin, C.-P., Weiskopf, N., Anwander, A., Jones, D. K., Rosen, B. R., Wald, L. L., and Huang, S. Y. (2022). Mapping the human connectome using diffusion mri at 300 mt/m gradient strength: Methodological advances and scientific impact. *NeuroImage*, 254:118958.

Fischl, B., Salat, D. H., van der Kouwe, A. J. W., Makris, N., Ségonne, F., Quinn, B. T., and Dale, A. M. (2004). Sequence-independent segmentation of magnetic resonance images. *NeuroImage*, 23:S69–S84.

Fukutomi, H., Glasser, M. F., Murata, K., Akasaka, T., Fujimoto, K., Yamamoto, T., Autio, J. A., Okada, T., Togashi, K., Zhang, H., Van Essen, D. C., and Hayashi, T. (2019). Diffusion tensor model links to neurite orientation dispersion and density imaging at high b-value in cerebral cortical gray matter. *Scientific Reports*, 9(1):12246.

Fukutomi, H., Glasser, M. F., Zhang, H., Autio, J. A., Coalson, T. S., Okada, T., Togashi, K., Van Essen, D. C., and Hayashi, T. (2018). Neurite imaging reveals microstructural variations in human cerebral cortical gray matter. *NeuroImage*, 182:488–499.

Ganepola, T., Nagy, Z., Ghosh, A., Papadopoulo, T., Alexander, D. C., and Sereno, M. I. (2018). Using diffusion mri to discriminate areas of cortical grey matter. *Neuroimage*, 182:456–468.

Glasser, M. F. and Essen, D. C. V. (2011). Mapping human cortical areas in vivo based on myelin content as revealed by t1- and t2-weighted mri. *Journal of Neuroscience*, 31(32):11597–11616.

Inverardi, F., Chikhladze, M., Donzelli, A., Moroni, R. F., Regondi, M. C., Pennacchio, P., Zucca, I., Corradini, I., Braida, D., Sala, M., Franceschetti, S., and Frassoni, C. (2013). Cytoarchitectural, behavioural and neurophysiological dysfunctions in the bcnu-treated rat model of cortical dysplasia. *European Journal of Neuroscience*, 37(1):150–162.

Jelescu, I. O., de Skowronski, A., Geffroy, F., Palombo, M., and Novikov, D. S. (2022). Neurite exchange imaging (nexi): A minimal model of diffusion in gray matter with inter-compartment water exchange. *NeuroImage*, 256:119277.

Kraguljac, N. V., Guerreri, M., Strickland, M. J., and Zhang, H. (2023). Neurite orientation dispersion and density imaging in psychiatric disorders: A systematic literature review and a technical note. *Biological Psychiatry Global Open Science*, 3(1):10–21.

Kroenke, C. D. (2018). Using diffusion anisotropy to study cerebral cortical gray matter development. *Journal of magnetic resonance (San Diego, Calif.: 1997)*, 292:106–116.

Lampinen, B., Zampeli, A., Björkman-Burtscher, I. M., Szczepankiewicz, F., Källén, K., Compagno Strandberg, M., and Nilsson, M. (2020). Tensor-valued diffusion mri differentiates cortex and white matter in malformations of cortical development associated with epilepsy. *Epilepsia*, 61(8):1701–1713.

Le Bihan, D. (2003). Looking into the functional architecture of the brain with diffusion mri. *Nature Reviews Neuroscience*, 4(6):469–480.

Lerch, J. P., Carroll, J. B., Dorr, A., Spring, S., Evans, A. C., Hayden, M. R., Sled, J. G., and Henkelman, R. M. (2008). Cortical thickness measured from mri in the yac128 mouse model of huntington's disease. *NeuroImage*, 41(2):243–251.

Leuze, C. W. U., Anwander, A., Bazin, P.-L., Dhital, B., Stüber, C., Reimann, K., Geyer, S., and Turner, R. (2014). Layer-specific intracortical connectivity revealed with diffusion mri. *Cerebral Cortex (New York, N.Y.: 1991)*, 24(2):328–339.

Lorente de Nó, R. (1938). Architectonics and structure of the cerebral cortex. In Fulton, J., editor, *Physiology of the Nervous System*. Oxford University Press.

Lorio, S., Adler, S., Gunny, R., D'Arco, F., Kaden, E., Wagstyl, K., Jacques, T. S., Clark, C. A., Cross, J. H., Baldeweg, T., and Carmichael, D. W. (2020). Mri profiling of focal cortical dysplasia using multi-compartment diffusion models. *Epilepsia*, 61(3):433–444.

Luhmann, H. J. (2016). Models of cortical malformation—chemical and physical. *Journal of Neuroscience Methods*, 260:62–72.

Luo, S., Zhou, J., Yang, Z., Wei, H., and Fu, Y. (2022). Diffusion mri super-resolution reconstruction via sub-pixel convolution generative adversarial network. *Magnetic Resonance Imaging*, 88:101–107.

McNab, J. A., Polimeni, J. R., Wang, R., Augustinack, J. C., Fujimoto, K., Player, A., Janssens, T., Farivar, R., Folkerth, R. D., Vanduffel, W., and Wald, L. L. (2013). Surface based analysis of diffusion orientation for identifying architectonic domains in the in vivo human cortex. *NeuroImage*, 69:87–100.

Moroni, R. F., Cipelletti, B., Inverardi, F., Regondi, M. C., Spreafico, R., and Frassoni, C. (2011a). Development of cortical malformations in bcnu-treated rat, model of cortical dysplasia. *Neuroscience*, 175:380–393.

Moroni, R. F., Zucca, I., Inverardi, F., Mastropietro, A., Regondi, M. C., Spreafico, R., and Frassoni, C. (2011b). In vivo detection of cortical abnormalities in bcnu-treated rats, model of cortical dysplasia, using manganese-enhanced magnetic resonance imaging. *Neuroscience*, 192:564–571.

Mountcastle, V. B. (1997). The columnar organization of the neocortex. *Brain: A Journal of Neurology*, 120 (Pt 4):701–722.

Nagy, Z., Alexander, D. C., Thomas, D. L., Weiskopf, N., and Sereno, M. I. (2013). Using high angular resolution diffusion imaging data to discriminate cortical regions. *PLOS ONE*, 8(5):e63842.

Najm, I., Lal, D., Alonso Vanegas, M., Cendes, F., Lopes-Cendes, I., Palmini, A., Paglioli, E., Sarnat, H. B., Walsh, C. A., Wiebe, S., Aronica, E., Baulac, S., Coras, R., Kobow, K., Cross, J. H., Garbelli, R., Holthausen, H., Rössler, K., Thom, M., El-Osta, A., Lee, J. H., Miyata, H., Guerrini, R., Piao, Y.-S., Zhou, D., and Blümcke, I. (2022). The ilae consensus classification of focal cortical dysplasia: An update proposed by an ad hoc task force of the ilae diagnostic methods commission. *Epilepsia*, 63(8):1899–1919.

Nazeri, A., Mulsant, B. H., Rajji, T. K., Levesque, M. L., Pipitone, J., Stefanik, L., Shahab, S., Roostaei, T., Wheeler, A. L., Chavez, S., and Voineskos, A. N. (2017). Gray matter neuritic microstructure deficits in schizophrenia and bipolar disorder. *Biological Psychiatry*, 82(10):726–736.

Nguyen, L. H. and Bordey, A. (2022). Current review in basic science: Animal models of focal cortical dysplasia and epilepsy. *Epilepsy Currents*, 22(4):234–240.

Nieuwenhuys, R. (2013). The myeloarchitectonic studies on the human cerebral cortex of the vogt-vogt school, and their significance for the interpretation of functional neuroimaging data. *Brain Structure & Function*, 218(2):303–352.

Novikov, D. S., Kiselev, V. G., and Jespersen, S. N. (2018a). On modeling. *Magnetic Resonance in Medicine*, 79(6):3172–3193.

Novikov, D. S., Veraart, J., Jelescu, I. O., and Fieremans, E. (2018b). Rotationally-invariant mapping of scalar and orientational metrics of neuronal microstructure with diffusion mri. *NeuroImage*, 174:518–538.

Palombo, M., Ianus, A., Guerreri, M., Nunes, D., Alexander, D. C., Shemesh, N., and Zhang, H. (2020). Sandi: A compartment-based model for non-invasive apparent soma and neurite imaging by diffusion mri. *NeuroImage*, 215:116835.

Püspöki, Z., Storath, M., Sage, D., and Unser, M. (2016). Transforms and operators for directional bioimage analysis: A survey. *Advances in Anatomy, Embryology, and Cell Biology*, 219:69–93.

Rakic, P. (2009). Evolution of the neocortex: a perspective from developmental biology. *Nature Reviews. Neuroscience*, 10(10):724–735.

Reveley, C., Ye, F. Q., Mars, R. B., Matrov, D., Chudasama, Y., and Leopold, D. A. (2022). Diffusion mri anisotropy in the cerebral cortex is determined by unmyelinated tissue features. *Nature Communications*, 13(11):6702.

Rojas-Vite, G., Coronado-Leija, R., Narvaez-Delgado, O., Ramírez-Manzanares, A., Marroquín, J. L., Noguez-Imm, R., Aranda, M. L., Scherrer, B., Larriva-Sahd, J., and Concha, L. (2019). Histological validation of per-bundle water diffusion metrics within a region of fiber crossing following axonal degeneration. *NeuroImage*, 201:116013.

Spocter, M. A., Hopkins, W. D., Barks, S. K., Bianchi, S., Hehmeyer, A. E., Anderson, S. M., Stimpson, C. D., Fobbs, A. J., Hof, P. R., and Sherwood, C. C. (2012). Neuropil distribution in the cerebral cortex differs between humans and chimpanzees. *Journal of Comparative Neurology*, 520(13):2917–2929.

Tournier, J.-D., Calamante, F., and Connelly, A. (2007). Robust determination of the fibre orientation distribution in diffusion mri: Non-negativity constrained super-resolved spherical deconvolution. *NeuroImage*, 35(4):1459–1472.

Tustison, N. J., Avants, B. B., Cook, P. A., Zheng, Y., Egan, A., Yushkevich, P. A., and Gee, J. C. (2010). N4itk: improved n3 bias correction. *IEEE transactions on medical imaging*, 29(6):1310–1320.

Veraart, J., Novikov, D. S., Christiaens, D., Ades-aron, B., Sijbers, J., and Fieremans, E. (2016). Denoising of diffusion mri using random matrix theory. *NeuroImage*, 142:394–406.

Villaseñor, P. J., Cortés-Servín, D., Pérez-Moriel, A., Aquiles, A., Luna-Munguía, H., Ramirez-Manzanares, A., Coronado-Leija, R., Larriva-Sahd, J., and Concha, L. (2023). Multi-tensor diffusion abnormalities of gray matter in an animal model of cortical dysplasia. *Frontiers in Neurology*, 14.

Vogt, C. and Vogt, O. (1919). *Allgemeine Ergebnisse unserer Hirnforschung*. J.A. Barth.

Walters, N. B., Egan, G. F., Kril, J. J., Kean, M., Waley, P., Jenkinson, M., and Watson, J. D. G. (2003). In vivo identification of human cortical areas using high-resolution mri: An approach to cerebral structure–function correlation. *Proceedings of the National Academy of Sciences*, 100(5):2981–2986.

Wong, M. (2009). Animal models of focal cortical dysplasia and tuberous sclerosis complex: Recent progress toward clinical applications. *Epilepsia*, 50(s9):34–44.

Yamaguchi, T., Kanemitsu, H., Yamamoto, S., Komatsu, M., Uemura, H., Tamura, K., and Shirai, T. (2010). N,n'-bis(2-chloroethyl)-n-nitrosourea (bcnu)-induced apoptosis of neural progenitor cells in the developing fetal rat brain. *Journal of Toxicologic Pathology*, 23(1):25–30.

Yoshida, S., Oishi, K., Faria, A. V., and Mori, S. (2013). Diffusion tensor imaging of normal brain development. *Pediatric radiology*, 43(1):15–27.

Yushkevich, P. A., Piven, J., Hazlett, H. C., Smith, R. G., Ho, S., Gee, J. C., and Gerig, G. (2006). User-guided 3d active contour segmentation of anatomical structures: significantly improved efficiency and reliability. *NeuroImage*, 31(3):1116–1128.

Zhang, H., Schneider, T., Wheeler-Kingshott, C. A., and Alexander, D. C. (2012). Noddi: practical in vivo neurite orientation dispersion and density imaging of the human brain. *NeuroImage*, 61(4):1000–1016.

A Supplementary Material

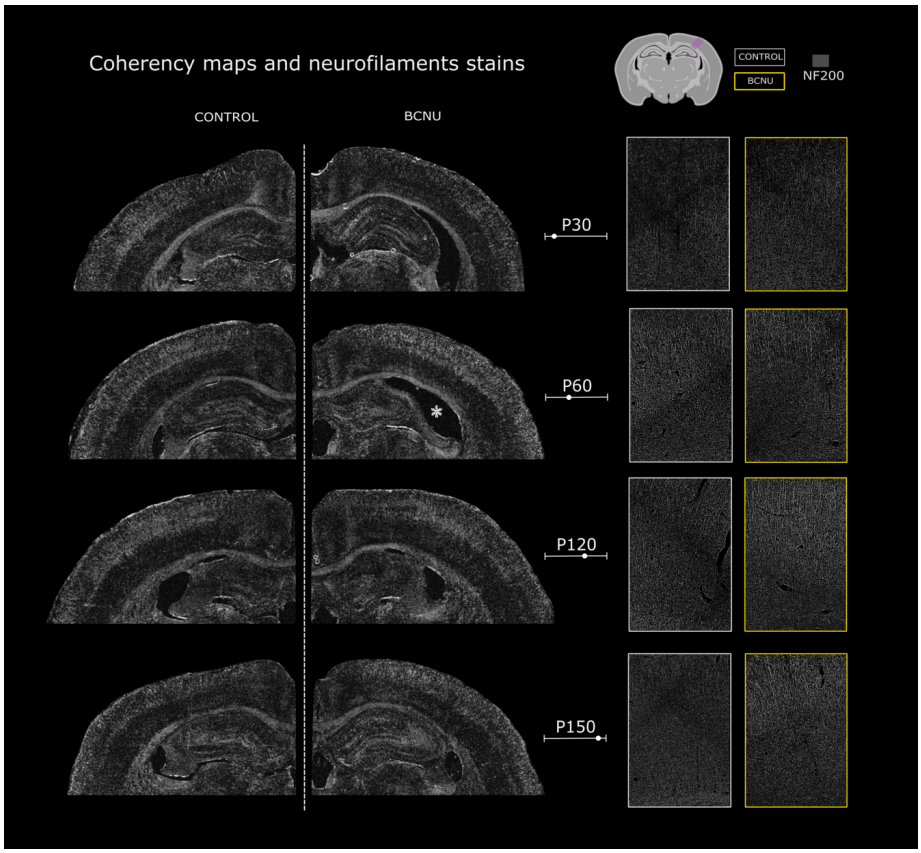

Figure A.1: *Evaluation of Neurofilaments. Left panel displays coherency maps estimated through the structure tensor using NF200 primary antibody stains. No significant differences in coherence or anisotropy patterns were observed between control and BCNU-treated animals. The right panel shows a close-up of the somatosensory cortex architecture, showing apparent normality between groups (controls in white rectangle; BCNU-treated rats in yellow rectangle) across all temporal time points.*